Biodegradable Monocrystalline Silicon Photovoltaic Microcells as Power Supplies for Transient Biomedical Implants

Luyao Lu, Zijian Yang, Kathleen Meacham, Caroline Cvetkovic, Elise A. Corbin, Abraham Vázquez-Guardado, Mantian Xue, Lan Yin, Javaneh Boroumand, Grace Pakeltis, Tian Sang, Ki Jun Yu, Debashis Chanda, Rashid Bashir, Robert W. Gereau IV, Xing Sheng,* and John A. Rogers*

Bioresorbable electronic materials serve as foundations for implantable devices that provide active diagnostic or therapeutic function over a timeframe matched to a biological process, and then disappear within the body to avoid secondary surgical extraction. Approaches to power supply in these physically transient systems are critically important. This paper describes a fully biodegradable, monocrystalline silicon photovoltaic (PV) platform based on microscale cells (microcells) designed to operate at wavelengths with long penetration depths in biological tissues (red and near infrared wavelengths), such that external illumination can provide realistic levels of power. Systematic characterization and theoretical simulations of operation under porcine skin and fat establish a foundational understanding of these systems and their scalability. In vivo studies of a representative platform capable of generating ≈60 µW of electrical power under 4 mm of porcine skin and fat illustrate an ability to operate blue light-emitting diodes (LEDs) as subdermal implants in rats for 3 d. Here, the PV system fully resorbs after 4 months. Histological analysis reveals that the degradation process introduces no inflammatory responses in the surrounding tissues. The results suggest the potential for using silicon photovoltaic microcells as bioresorbable power supplies for various transient biomedical implants.

Implantable electronic devices play crucial roles in delivering therapy and recording physiological information in both animal models and humans, with broad relevance in areas ranging from biological research to clinical medicine.[1,2] Examples include the cardiac pacemaker, for control of abnormal heart rhythms,[3] and the deep brain stimulator, for treatment of disabling neurological diseases.[4] These and other related devices typically require operation over the lifetime of the patient. Other possibilities for electronic implants demand function only for a period matched to a transient biological process, such as wound healing. Here, the use of bioresorbable materials may allow for classes of devices that simply disappear into the body after the required time for their operation. Previous studies show that water soluble materials, such as monocrystalline silicon (Si), metals (Mg, Mo, Fe, Zn, and W), metal oxides (SiO_2, MgO, and Si_3N_4), and organic polymers (silk fibroin

Dr. L. Lu, Z. Yang, M. Xue, G. Pakeltis, T. Sang
Department of Materials Science and Engineering
and Frederick Seitz Materials Research Laboratory
University of Illinois at Urbana–Champaign
Urbana, IL 61801, USA

Dr. L. Lu
Center for Bio-Integrated Electronics at the Simpson Querrey Institute
for BioNanotechnology
and the Department of Materials Science and Engineering
Northwestern University
Evanston, IL 60208, USA

Dr. K. Meacham, Prof. R. W. Gereau IV
Washington University Pain Center
and Department of Anesthesiology
Washington University School of Medicine
St. Louis, MO 63110, USA

[+]Present address: Center for Neuroregeneration, Houston Methodist
Research Institute, Houston, TX 77030, USA

[++]Present address: Cardiovascular Institute, Perelman School of
Medicine, University of Pennsylvania, Philadelphia, PA 19104, USA

DOI: 10.1002/aenm.201703035

Dr. C. Cvetkovic,[+] Dr. E. A. Corbin,[++] Prof. R. Bashir
Department of Bioengineering
University of Illinois at Urbana–Champaign
Urbana, IL 61801, USA

A. Vázquez-Guardado, Dr. J. Boroumand, Prof. D. Chanda
CREOL
The College of Optics and Photonics
and NanoScience Technology Center
University of Central Florida
Orlando, FL 32826, USA

Prof. L. Yin
School of Materials Science and Engineering
Tsinghua University
Beijing 100084, China

Prof. K. J. Yu
School of Electrical and Electronic Engineering
Yonsei University
Seoul 03722, Republic of Korea

Prof. X. Sheng
Department of Electronic Engineering
Tsinghua University
Beijing 100084, China
E-mail: xingsheng@tsinghua.edu.cn

and collagen) can serve as the basis for broad classes of active and passive bioresorbable components, such as transistors, capacitors, resistors, diodes, inductors, radio frequency antennas, batteries, and chemical/physical sensors. Integrated collections of these components yield systems with realistic levels of function for applications ranging from intracranial monitors, to thermal therapeutics and drug release vehicles to radio frequency tags and sensors.[5–13] In all cases, an ideal platform for applications in temporary biomedical implants must combine, at a minimum, a sensor and/or actuator and a source of power, for which all constituent materials are fully bioresorbable and biocompatible. Such platforms are free of additional psychological complications associated with pain, bleeding, and other risks from the secondary surgical extraction process.[14,15]

Despite significant advances in this area, a key remaining challenge is in power supply. One option is in mechanical and radio frequency (RF) energy harvesting. As an example of the former, Dagdeviren et al.[16] demonstrated devices based on thin films of ZnO as the piezoelectric material, capable of producing output voltages and currents in the range of ≈1 V and ≈0.5 nA for physiologically relevant types of motions. As an example of the latter, Hwang et al.[6] reported near and far field RF harvesters with antennas of Mg designed to operate at ≈2.4 GHz and ≈950 MHz, with demonstrations of wireless operation of LEDs at distances of up to ≈2 m. Although promising, each of these approaches has some combination of disadvantages in their relatively large sizes, the modest levels of power that they can produce and/or their limited ability to operate effectively over relevant time periods as implants. Many applications, such as powering pacemakers and LEDs, require compact devices capable of yielding tens of microwatts or milliwatts of power with fully biocompatible construction.
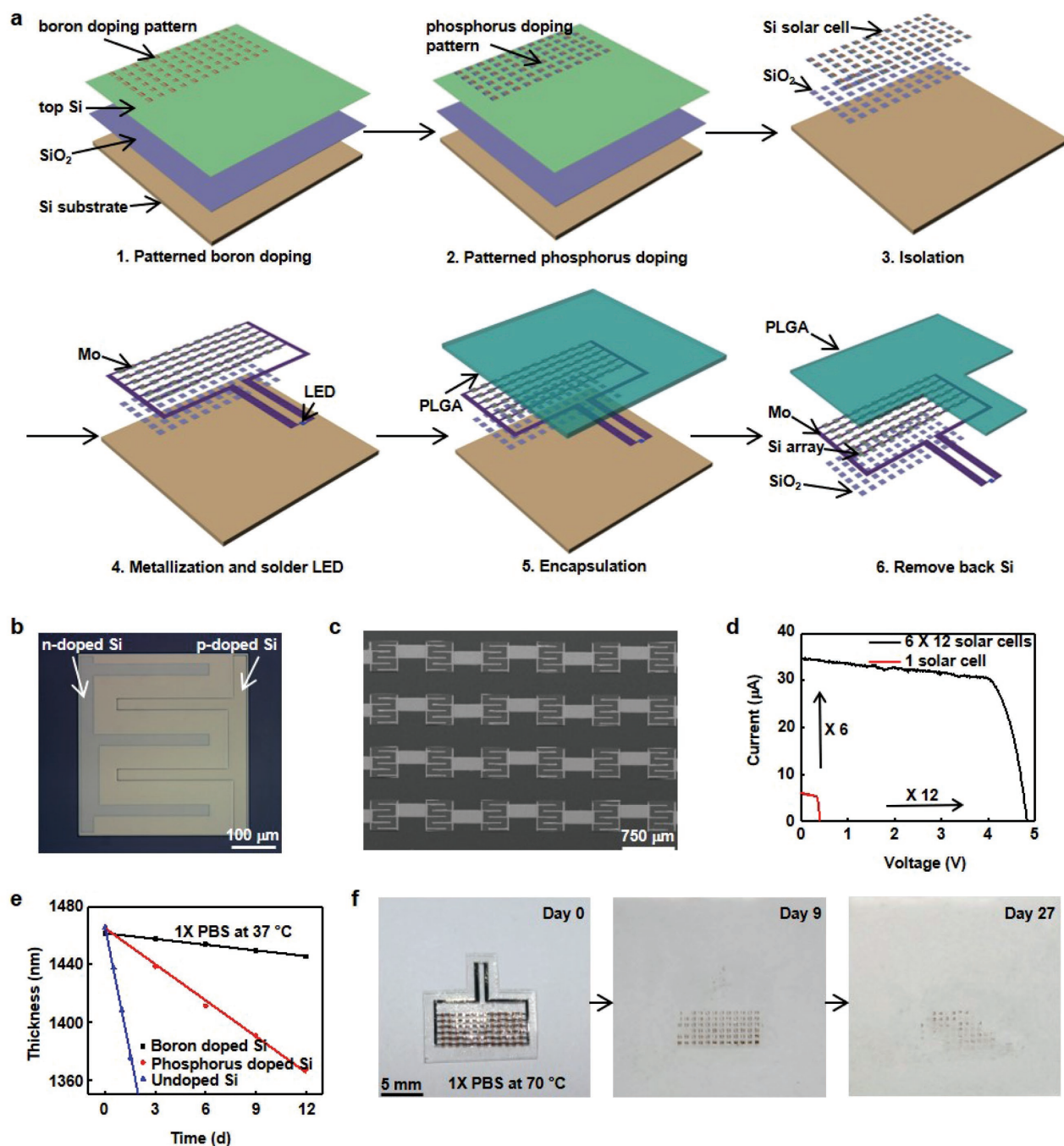
Photovoltaic (PV) cells represent an interesting possibility, with potential ability to meet these requirements. Previous work shows that commercial, nonresorbable solar cells placed subdermally can produce sufficient power to operate pacemakers inside the body.[17,18] Kang et al. reported bioresorbable forms of thin-film solar cells based on amorphous silicon and Mg electrodes, but with efficiencies much lower than those possible with monocrystalline silicon and with inability to operate in an aqueous environment for more than a few hours, which limits their applications as practical in vivo power supplies.[19] Early reports suggest promise of higher efficiencies by use of silicon microcells similar to those first described in the context of high performance flexible photovoltaics.[5,20] Here, we demonstrate materials and design strategies for an ultrathin integrated solar cell array based on monocrystalline silicon microcells as a power supply, in which all the components, including active layer, electrodes, interconnections, and encapsulation layers

Prof. J. A. Rogers
Center for Bio-Integrated Electronics
Departments of Materials Science and Engineering, Biomedical Engineering, Chemistry, Mechanical Engineering, Electrical Engineering and Computer Science, and Neurological Surgery
Simpson Querrey Institute for Nano/Biotechnology
McCormick School of Engineering and Feinberg
School of Medicine Northwestern University
Evanston, IL 60208, USA
E-mail: jrogers@northwestern.edu

exploit fully biocompatible and biodegradable materials. When exposed to 1 sun illumination, a representative array generates approximately 122 μW with an open circuit voltage (V_{oc}) of 4.84 V, and an output of 64 μW, and a V_{oc} of 4.25 V under near-infrared (NIR) illumination beneath a 4 mm thick piece of porcine skin and fat. These values reach levels that are comparable to those of conventional, nonresorbable subdermal PV devices.[17,18,21] The output voltage and current can be adjusted through the network geometry of series and parallel interconnects between the microcells. In vitro cytotoxicity tests reveal that these systems are fully biocompatible. Intermittent operation of an implanted LED for 3 d subcutaneously in rats serves as a proof-of-concept in vivo demonstration. The integrated device fully dissolves in the infrascapular region after 4 months of implantation. Histological evaluation shows that the dissolution process introduces no inflammatory reactions in the surrounding tissues. To the best of our knowledge, these results represent the first in vivo demonstration of fully biodegradable photovoltaic systems as power sources, with implications for use in bioresorbable electronic implants.

Figure 1a presents a schematic illustration of the fabrication strategy. The process starts with a silicon on insulator (SOI) wafer with top Si layer, buried oxide layer, and Si substrate thicknesses of 1.5, 3, and 200 μm, respectively. The first step involves thermal oxidation to produce a layer of SiO_2 (100 nm) on the top Si, as a photolithographically patterned hard mask for doping with boron (Boron, BN-1250, Saint-Gobain) and phosphorus (Phosphorus, PH-1000N, Saint-Gobain) at 1000 °C for 30 and 6 min (concentrations ≈10^{20} cm^{-3}), respectively.[10] Figure S1 (Supporting Information) presents the doping geometry for a single microcell. Photolithography and reactive ion etching (SF_6, 40 sccm, 50 mTorr, 100 W, and 3 min) define the structure of an array of isolated silicon microcells. Immersion in hydrofluoric acid (HF) removes the buried oxide layer in the regions between the microcells. Photolithographically patterned metallization (Mo, 1.5 μm) serves as electrodes and interconnections for the array. Soldering an LED onto Mo contact pads that connect to this array provides a visual indicator of device operation for studies as implants, as discussed in detail later. Drop-casting of a layer of poly(lactic-co-glycolic acid) (PLGA) at a thickness of ≈200 μm and lactide/glycolide ratio of 65:35, followed by melting at 150 °C for 4 h yields a biodegradable substrate and encapsulation coating. Removal of the silicon wafer by backside etching completes the fabrication process. Here, the remaining buried oxide layer underneath the microcells serves as a back biofluid barrier for the array. For the studies reported here, each array includes 72 solar cells, in 12 columns connected in series, and 6 rows in parallel. Additional details are in the Experimental Section.

Figure 1b provides an optical image of an individual microcell, showing the interpenetrating patterns of boron and phosphorus doping. The dimensions are 390 μm × 410 μm × 1.5 μm. Figure 1c presents a scanning electron microscope (SEM) image of 24 Si solar cells from the array. The Mo interconnections between microcells have dimensions of 180 μm × 350 μm × 1.5 μm. Figure 1d presents the current versus voltage characteristics measured from a single microcell and an array under simulated AM 1.5G solar irradiance at room temperature. The single cell shows a power conversion efficiency of 1.29% with

ADVANCED
SCIENCE NEWS
www.advancedsciencenews.com

ADVANCED
ENERGY
MATERIALS
www.advenergymat.de

Figure 1. Bioresorbable, monocrystalline silicon microcell photovoltaics. a) Schematic illustration of key fabrication steps. b) Optical image of a single microcell. Scale bar, 100 μm. c) Top view SEM image of 24 interconnected microcells (4 × 6) from the array. Scale bar, 750 μm. d) Current/voltage characteristics of a single microcell (red) and an interconnected array (black). e) Changes in thickness of silicon as a function of time of immersion in 1× PBS solution (pH 7.4, Mediatech Inc.) at 37 °C for boron doped (black), phosphorus doped (red), and undoped (blue) material. f) Sequence of images collected at different days, showing accelerated dissolution of a bioresorbable Si PV array in 1× PBS solution (pH 7.4, Mediatech Inc.) at 70 °C. Scale bar, 5 mm.

a short circuit current density (J_{sc}) of 4.37 mA cm^{-2}, a V_{oc} of 0.40 V, and a fill factor (FF) of 73.3%, respectively. The average J_{sc}, V_{oc}, and FF values over 20 single solar cells are 4.34 ± 0.04 mA cm^{-2}, 0.40 ± 0.01 V, and 73 ± 1%, respectively. The array design increases the V_{oc} to 4.84 V with a short circuit current (I_{sc}) of 34.45 μA, for a total output power of 122 μW, which is slightly lower than the expected output power based

on the single microcell behavior (128 μW) due to cell variabilities and contact resistances.[20] Optical absorption through these thin cells limits their performance compared to that of conventional silicon devices (100 − 200 μm thickness).[22–24] Increasing the Si thickness can improve the performance, but at the expense of extending the time for bioresorption through hydrolysis.

**ADVANCED
SCIENCE NEWS**
www.advancedsciencenews.com

**ADVANCED
ENERGY
MATERIALS**
www.advenergymat.de

The chemical kinetics of this hydrolysis reaction is critically important to the use of silicon in the applications contemplated here. The reaction involves conversion of silicon into silicic acid, with a rate that strongly depends on the doping level of the silicon, as well as the pH and chemical composition (e.g., ion type and concentration) of the environment, and its temperature.[5,7,25,26] Figure 1e illustrates the dissolution kinetics of boron doped, phosphorus doped, and undoped Si (initial thickness ≈1460 nm) captured by measuring the changes in thickness as a function of time, using an SOI wafer immersed in 1 × phosphate buffered saline (PBS) solution (pH 7.4, Mediatech Inc.) at physiological temperature (37 °C). Boron doped, phosphorus doped, and undoped Si all show linear dissolution kinetics with rates of ≈1.3 ± 0.03, 8.3 ± 0.2, and 58 ± 1 nm d^{-1}, respectively. The dissolution rates are comparable to previous reported values for silicon nanomembranes, ranging from a few nanometers to 100 nm d^{-1}; differences might arise from differences in conditions such as concentrations and types of ion in the solution.[5,7,26]

The dissolution characteristics of other materials in these systems, i.e., Mo, SiO$_2$, and PLGA, are also important. Previous reports show that Mo and SiO$_2$ dissolve in biofluids with rates of ≈25 and 8 nm d^{-1} at pH 7.4 and body temperature, while PLGA layer degrades in ≈1–2 months.[8,10,27] Figure 1f presents a set of images of an integrated system collected during accelerated dissolution studies (1× PBS solution

at pH 7.4 and 70 °C, Mediatech Inc.). The Mo electrodes dissolve first, within 9 d, followed by the Si and SiO$_2$ over the following several weeks. Areas of undoped Si dissolve more quickly than those doped with phosphorus; the regions of boron doping dissolve most slowly, consistent with the results in Figure 1e. All materials exhibit increased rates of dissolution at elevated temperatures compared to physiological values, as expected. For example, the dissolution rate for undoped Si increases from ≈58 ± 1 nm d^{-1} at 37 °C to ≈590 ± 20 nm d^{-1} at 70 °C in 1× PBS solution (pH 7.4, Mediatech Inc., Figure S2, Supporting Information). The calculated activation energy based on the Arrhenius equation is ≈0.6 eV, consistent with literature values.[25]

The optical properties of biological tissues in general, and layers of skin in particular, are important to consider. Porcine skin has many features that are similar to those of human skin, such as thickness, general structure, pigmentation, collagen composition, and thus widely serves as a preclinical model.[28] **Figure 2**a demonstrates the transmission spectra for a sample of porcine skin (thickness ≈2 mm) and fat (thickness ≈2 mm). Although only 0–20% of incident light from 400 to 500 nm passes through the porcine skin, the transmission gradually increases to ≈60% at 800 nm and remains at between 60–65% up to 1100 nm. Placing fat under the skin contributes to an additional loss of 0–25% for wavelengths between 400 and 1100 nm.
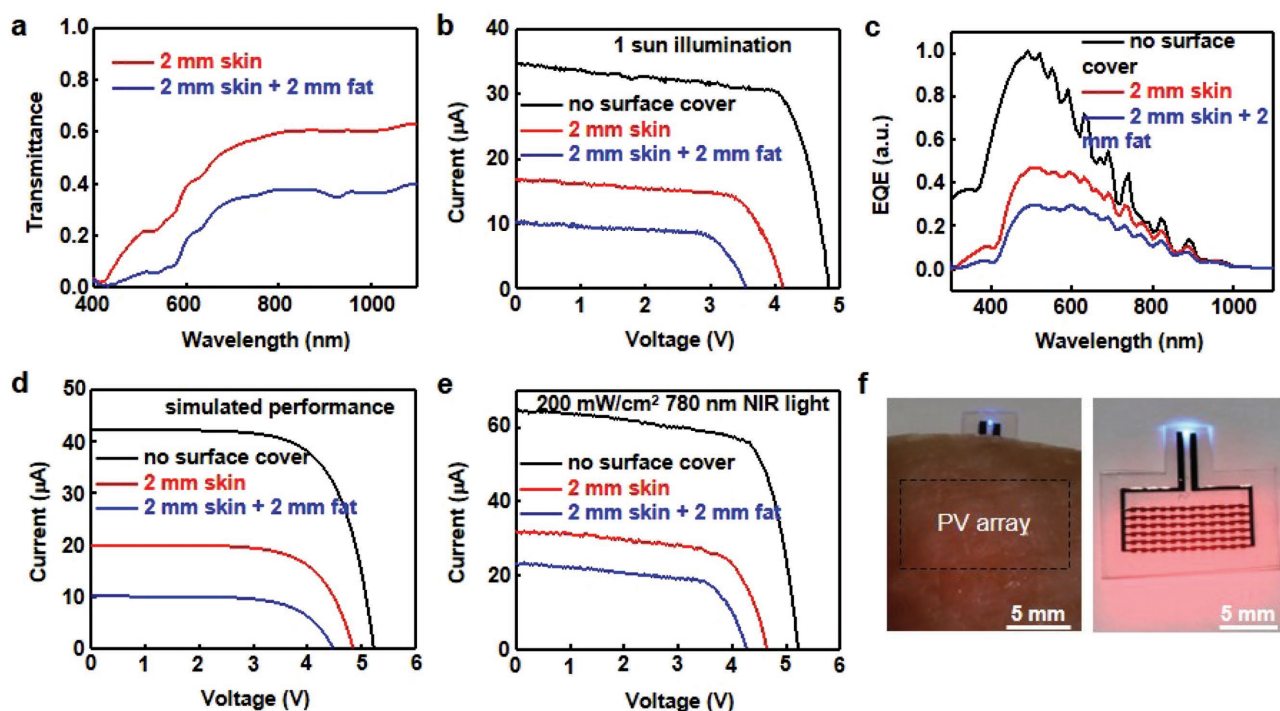
Figure 2. Photovoltaic performance of the bioresorbable Si PV array. a) Transmission spectra of 2 mm porcine skin (red), and skin with 2 mm fat (blue). b) Current/voltage characteristics of an array measured under 1 sun illumination (black), with skin on its surface (red), with skin and fat on its surface (blue), respectively. c) Normalized EQE spectra of a microcell measured in the same three scenarios as illustrated in (b). d) Simulated current versus voltage curves of an Si solar array under different conditions in (b). e) Current/voltage curves of an array measured during exposure to 200 mW cm^{-2} from an NIR LED light with different materials on its surface. f) Optical images of the use of an Si PV system to operate a blue LEDs during exposure to 200 mW cm^{-2} NIR illumination. (Left) A functioning device under pig skin and fat. (Right) A functioning device after immersion in 1× PBS solution (pH 7.4, Mediatech Inc.) at 37 °C for 5 d. Scale bar, 5 mm.

**ADVANCED
SCIENCE NEWS**
www.advancedsciencenews.com

**ADVANCED
ENERGY
MATERIALS**
www.advenergymat.de

Figure 2b shows the current–voltage characteristics of an array with and without porcine skin and fat on top, for the case of 1 sun illumination of 100 mW cm^{-2}. Compared to the case of a bare array, the I_{sc} decreases from 34.45 to 16.66 µA, and further to 10.34 µA while V_{oc} decreases from 4.84 to 4.11 V, and further to 3.55 V for the cases of skin and skin with fat, respectively. As a result, the overall output power decreases from 122 to 47.9 µW, and finally to 25.0 µW, for these cases, respectively. Table S1 (Supporting Information) summarizes the average photovoltaic performance of 20 arrays under different surface covers. The average output power decreases from 120 ± 4 to 47 ± 1 µW, and further to 25 ± 1 µW, respectively. Figure 2c presents the external quantum efficiency (EQE) for a single microcell. Skin and fat introduce significant decreases in EQE from 500 to 700 nm, consistent with the losses in Figure 2a. The V_{oc} depends on the optical generation rate, which is qualitatively consistent with this observed decrease in V_{oc} ($\approx$14%) under skin and skin with fat.[29]

Computational modeling provides quantitative insights into these measurement results. Optical simulations reveal that the optical power density from 400 to 1100 nm for simulated AM 1.5G solar irradiance decreases from 75.85 to 31.46 and 17.37 mW cm^{-2} through 2 mm skin, and 2 mm skin with 2 mm fat, respectively. Figure 2d summarizes the simulation results for a microcell array with these different materials on top. The bulk recombination lifetime and surface recombination velocity for the results in Figure 2d are 1 µs and 10^3 cm s^{-1}, respectively, similar to previously reported values.[30,31] The array exhibits an I_{sc} of 42.21 µA, a V_{oc} of 5.28 V, and an FF of 68.46% directly under illumination. I_{sc} and V_{oc} decrease to 20.05 µA and 4.80 V under the skin and further to 10.17 µA and 4.44 V under skin with fat, respectively. As a result, output power of the silicon microcell array decreases from 152.58 to 64.78 µW, and finally to 29.83 µW, respectively. Differences between measured and simulated results mainly arise from resistive losses and contact shadows. Overall, the simulated changes in output power under tissues ($\approx$43% and $\approx$20% of the bare array output power remains under the skin, and the skin with fat, respectively) match well with the measured changes ($\approx$39% and $\approx$19% of the bare array output power remains under the skin, and the skin with fat, respectively) in Figure 2b. Details of the simulation approaches are in the Experimental Section.

Since the skin exhibits a relatively high transmission for NIR light (Figure 2a), an NIR LED (M780L3, Thorlabs) with an emission maximum at 780 nm (and full width at half maximum, FWHM, at 28 nm; Figure S3, Supporting Information) represents a good choice as a portable light source to deliver power to the array. Figure 2e presents the performance under an optical power density of 200 mW cm^{-2} from the NIR LED. Optical simulations show that the power decreases to 116.88 and 73.51 mW cm^{-2} under skin without and with fat, respectively. The array generates 242 µW under direct illumination, 96.4 µW under skin, and 64.4 µW under skin with fat, while the V_{oc} decreases from 5.23 to 4.64 V and finally to 4.25 V for these conditions, respectively (Figure 2e). This power level is sufficient to operate devices, such as LEDs and pacemakers in the body.[21,32] Note that the PLGA shows a high transmission rate (>98%) for wavelengths between 580 and 800 nm (Figure S4,

Supporting Information) and thus, has little influence on the performance of the array.

Figure 2f (left) demonstrates the use of an array under pig skin with fat for activating a blue LED with a turn-on voltage of 2.7 V (Figure S5, Supporting Information). The array functions in a stable fashion after immersion in 1 × PBS solution (pH 7.4, Mediatech Inc.) at 37 °C for 5 d before device failure, as illustrated in Figure 2f (right), limited only by the timescale for dissolution and water penetration through the PLGA encapsulation. Increasing the thickness of this encapsulation and/or developing materials with slower degradation kinetics will increase the lifetime.[33]

Cytotoxicity tests with human umbilical vein endothelial cells (HUVECs) seeded and cultured on a PV substrate with geometry shown in Figure S6 in Supporting Information (2000 µm × 4000 µm × 1.5 µm) reveals its biocompatibility. Details of these tests are in the Experimental Section. HUVECs are an attractive cell choice for such studies because of their physiological relevance. **Figure 3**a shows the growth and proliferation behaviors of cells, as depicted by a set of fluorescent images (lower), complemented by differential interference contrast image counterparts (upper) on days 1, 4, and 7. Overall, the presence of well-spread and flattened cells with overall viability between 89% and 91% is consistent with an absence of any toxic effects (Figure 3b). Figure 3c shows the numbers of live (green) and dead (red) cells. Throughout the duration of the experiment, the numbers of dead cells are significantly lower than that of the live cells, thereby providing evidence of good biocompatibility. The significant increase in numbers of live cells between day 1 and day 4 indicates proliferation across the solar cell surface, with no significant difference between days 4 and 7.

Operating a blue LED with the PV array embedded in the infrascapular region of an adult Sprague-Dawley rat represents a proof-of-the-concept example of functionality as a bioresorbable power source for biomedical electronics. All animal experiment procedures follow institutionally approved protocols. **Figure 4**a shows the steps for surgical implantation. The process begins with administration of isoflurane anesthesia. Subcutaneous implantation in the region between the shoulder blades involves sterile techniques. A straight incision opens the area for device insertion. Stitching the wound area completes the surgery. The device sustains functioning for 3 d after implantation. Figure 4b shows an optical image of operation of an LED powered by an implanted Si PV array during NIR illumination on day 3 after the surgery. Protocols for exposure to low intensity NIR light are similar to those for low level NIR therapy used widely for muscle repair and pain relief.[34] The effective conversion of NIR light to blue light using these systems might have direct relevance in optogenetic techniques for studies of neural function.[35]

Figure 4c shows an image of the subcutaneous region captured with the animal under anesthesia after 4 months. The rat displays no signs of disease or debilitation during this time and little/no device residues are apparent under visual and optical microscope evaluation. Figure 4d (left and middle) presents results of standard hematoxylin and eosin (H&E) staining of the subcutaneous tissue immediately adjacent to the implanted device after its complete dissolution, as an assay for signs of gross infiltration of neutrophils, lymphocytes, monocytes,
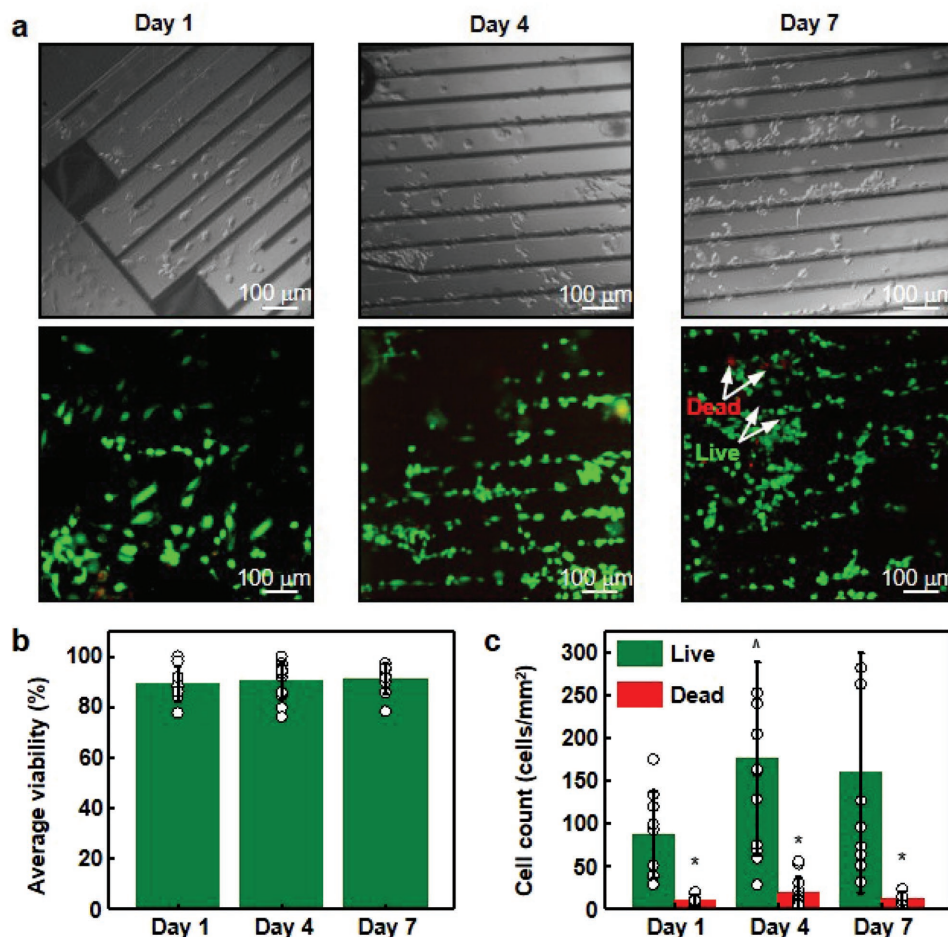
Figure 3. In vitro cytotoxicity test of bioresorbable Si PV arrays. a) Phase contrast (upper) and fluorescent (lower) images of the microcells at different time points. In a LIVE/DEAD viability assay, living cells produce green fluorescence and dead cells produce red fluorescence. Scale bar, 100 μm. b) The average viability (percent of living cells) at different time points. c) Cell count (number of cells per area) at different time points. For all days, the number of dead cells is significantly decreased (*) compared to live cells. The number of live cells is significantly increased between days 1 and 4 (^). Data are collected from 9–12 regions per time point, from which there are three microcells each. Results are presented as mean ± SD. One-way analysis of variance statistical testing is followed by Tukey's multiple comparison test for $p < 0.05$.
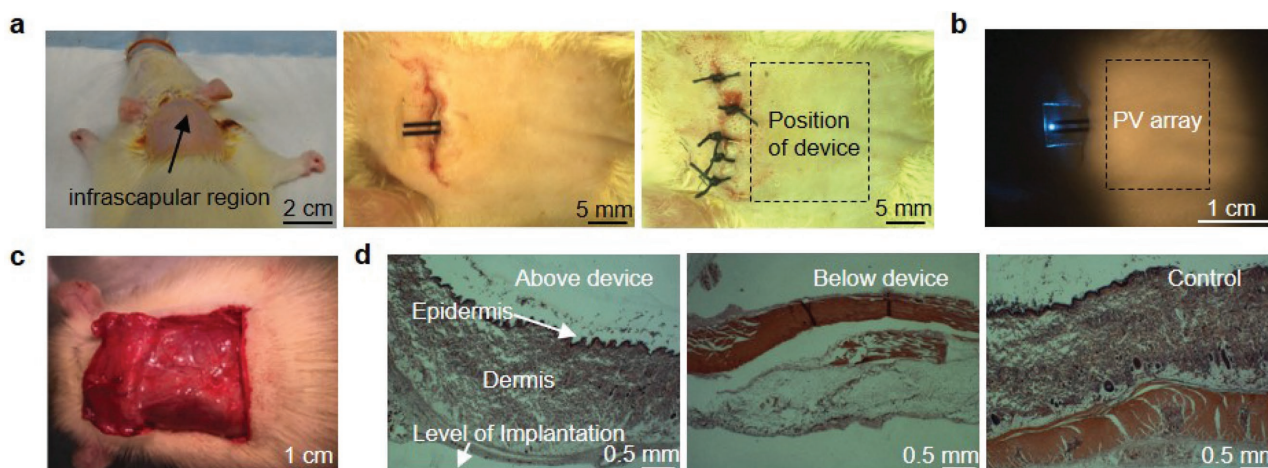
Figure 4. Application of bioresorbable PV systems as implants in rats. a) Optical images during the surgical procedure for implantation in the infrascapular region. b) Operation of a blue LED powered by the PV array on postimplantation day 3, during exposure to NIR illumination. Scale bar, 1 cm. c) Optical image of the infrascapular region with a PV system implanted for 4 months, showing that the device has fully dissolved. Scale bar, 1 cm. d) Standard H&E staining of subcutaneous tissues. (Left) above, (middle) below the site of device implantation. (Right) from a naïve control rat in the same region. Scale bar, 0.5 mm.

ADVANCED
SCIENCE NEWS
www.advancedsciencenews.com

ADVANCED
ENERGY
MATERIALS
www.advenergymat.de

basophils, eosinophils, red blood cells, or lipofuscin. As compared with naïve rat subcutaneous tissue from the same region (Figure 4d, right), no major differences in skin thickness, nor signs of immune cell infiltration at the implantation site are apparent, which indicates that the degradation process and its by-products are biocompatible.

Fully transient bioelectronic systems offer new opportunities for advanced tools in biological research and biomedical devices in clinical medicine. The work presented here introduces a fully bioresorbable system for wirelessly powering transient electronic implants in live animals, with ability to generate sufficient power to operate LEDs in a stable fashion for several days, where complete dissolution and bioresorption occurs in several months. The microcell architecture allows the output currents and voltages to be selected over a wide range, to satisfy diverse requirements in implantable devices of various types. Detailed studies show that this type of system and the products of its dissolution in biofluids are biocompatible. These results provide an attractive solution for the challenge of in vivo power supply for bioresorbable electronic systems, thereby accelerating the development of different classes of temporary implants, with application possibilities that range from cardiac pacing to enhance outcomes from surgical recovery to electrical stimulation to accelerate the rates of healing of bone fractures.[36]

Experimental Section

Fabrication of the Device: Fabrication began with growth of a layer of SiO_2 (≈100 nm) on an SOI wafer (top Si thickness ≈1.5 μm, SOITEC) by thermal oxidation. Etching the SiO_2 in buffered oxide etch (BOE) through a photolithographically patterned mask of photoresist (AZ 5214, Microchem) opened areas for doping with boron (Boron, BN-1250, Saint-Gobain) at 1000 °C for 30 min. Immersion in BOE for 3 min then completely removed the SiO_2. Phosphorus doping (Phosphorus, PH-1000N, Saint-Gobain) followed similar procedures, at 1000 °C for 6 min. Photolithography and reactive ion etching (SF6, 40 sccm, 50 mTorr, 100 W, and 3 min) through a photoresist mask (AZ 5214, Microchem) removed selected regions of the top Si layer (1.5 μm). Immersion in concentrated HF for 1.5 min completely removed the buried oxide layer. Photolithography (AZ nLOF 2070, Microchem) and liftoff in acetone defined Mo (thickness ≈1.5 μm) electrodes and interconnects. An In/Ag solder paste (Indalloy 290, Indium Corporation) allowed electrical connections between an LED at the Mo interconnects. Transferring an LED (C460TR2227-0216, Cree Inc.) onto the paste followed by heating at 150 °C for 2 min served to establish these connections. Drop-casting PLGA in acetone solution (weight ratio 10%) on the wafer, followed by melting at 150 °C for 4 h formed an encapsulation layer (thickness ≈200 μm). XeF₂ etching removed the bottom Si substrate and completed the fabrication.

Photovoltaic Measurement: Measurements with a Keithley 2400 sourcemeter defined the performance of the Si solar cell array. The illumination source was an Oriel 91192-1000W Solar Simulator with an AM 1.5G filter and power density at 100 mW cm⁻².

Optical Simulations: Modeling of the optical response of the silicon solar cell used the finite difference time domain method (FDTD, Lumerical Inc.) to obtain the carrier generation rate in the volume of the cell as a result of optical absorption, with normalization to the spectral irradiance of the source at the surface of the silicon. The two external sources included: the solar spectrum (AM 1.5G) with 75.85 mW cm⁻² irradiance in the 400–1100 nm wavelength band and an NIR LED with 200 mW cm⁻² irradiance, 780 nm peak wavelength, and 28 nm FWHM. For a solar cell underneath porcine skin/fat tissue (refractive index ≈1.4), the transmission through the biological tissue

reduced the incident spectral irradiance at the silicon interface, hence reducing the carrier generation rate. Transmission through 2 mm of skin (Figure 2a) reduced the power of the solar and NIR LED irradiance sources to 31.46 and 116.88 mW cm⁻², respectively. Transmission through 2 mm of skin and 2 mm of fat further reduced the power of the solar and NIR LED irradiance sources to 17.37 and 73.51 mW cm⁻², respectively.

Electrical Simulations: The electrical simulations used the finite element method (DEVICE, Lumerical Inc.). The calculated generation rate obtained numerically using FDTD served as the source of local carriers in the electrical simulations for each source excitation and biological tissue configuration. The doping concentrations were 10^{20} cm⁻³ with a geometry described in Figure 2b. Molybdenum served as the contacts. The surface recombination velocity was set to 10^3 cm s⁻¹ and the bulk carrier lifetime was set to 1 μs.

Cell Culture and Biocompatibility Studies: Directly fabricating and attaching a removable microincubation chamber (≈50 μL) to the solar cells allowed for adherent cell seeding and culturing, as described previously. Rinsing with 70% ethanol and then with PBS cleaned the interior regions of the chamber wells before cell seeding and culturing. Cell culturing used endothelial cell basal medium-2 (EBM-2, Lonza) with EGM-2 SingleQuots growth supplement kit (Lonza). For seeding onto the solar cells, HUVECs were lifted from a T-75 cell culture flask with 0.25% trypsin-ethylenediaminetetraacetic acid (Gibco), centrifuged at 200 × *g* for 5 min, resuspended in culture media, and seeded at a concentration of ≈300 cells mm⁻² in the well of each microincubation chamber. A sterile coverslip sealed the well and prevented evaporation of the fluid. Solar cells with HUVECs remained in an incubator at 37 °C and 5% CO_2 for 24 h before removal of the coverslip and microincubation wells using clean forceps. The solar cells with HUVECs remained in a sterile 35 mm dish containing 3 mL of fresh media as culturing continued for the duration of the experiment. An immunofluorescence live/dead assay (Invitrogen) performed on days 1, 4, and 7 determined the viability of the HUVECs and the cytotoxicity of the solar chip substrates. On the appropriate days, substrates with HUVECs were incubated in the dark at room temperature with calcein AM (1 × 10⁻⁶ M) and ethidium homodimer (2 × 10⁻⁶ M) in PBS for 45 min, rinsed three times with PBS, and immediately imaged. The presence of intracellular esterase activity produced an intense green fluorescence to identify the living cells while the binding of the ethidium homodimer to the nucleic acids of cells with damaged membranes produced a red fluorescence to identify dead cells. Cell viability (%) corresponds to the number of living (green) cells compared to the total number of cells, quantified using ImageJ software.

In Vivo Biocompatibility Study: The Animal Care and Use Committee of Washington University approved all procedures for this study. A male Sprague-Dawley rat, induced and maintained with inhalational anesthesia, was shaved with razor and depilatory cream across its upper back/infrascapular region. The implantation occurred under sterile conditions. The rat was housed and fed under standard conditions both prior to and after implantation. Following 4 months of implantation, visual examination of the subcutaneous space with the rat under inhalational anesthesia confirmed complete dissolution of the device. After administration of ketamine, xylazine, and acepromazine, the rat underwent transcardial perfusion with PBS and then 4% paraformaldehyde. The tissues were embedded in paraffin and cut into approximately 5 μm sections. Random sections were stained with H&E and inspected using optical microscopy for qualitative evaluation of differences in skin thickness or immune cell infiltration, as compared with similarly prepared and stained tissue from a naïve male Sprague-Dawley rat.

Supporting Information

Supporting Information is available from the Wiley Online Library or from the author.

[1] Y. Hao, R. Foster, *Physiol. Meas.* **2008**, *29*, R27.

[2] J. P. DiMarco, *N. Engl. J. Med.* **2003**, *349*, 1836.

[3] J. D. Fisher, S. G. Kim, S. Furman, J. A. Matos, *Am. J. Cardiol.* **1982**, *49*, 194.

[4] J. A. Obeso, C. W. Olanow, M. C. Rodriguez-Oroz, P. Krack, R. Kumar, A. E. Lang, *N. Engl. J. Med.* **2001**, *345*, 956.

[5] S.-W. Hwang, H. Tao, D.-H. Kim, H. Cheng, J.-K. Song, E. Rill, M. A. Brenckle, B. Panilaitis, S. M. Won, Y.-S. Kim, Y. M. Song, K. J. Yu, A. Ameen, R. Li, Y. Su, M. Yang, D. L. Kaplan, M. R. Zakin, M. J. Slepian, Y. Huang, F. G. Omenetto, J. A. Rogers, *Science* **2012**, *337*, 1640.

[6] S.-W. Hwang, X. Huang, J.-H. Seo, J.-K. Song, S. Kim, S. Hage-Ali, H.-J. Chung, H. Tao, F. G. Omenetto, Z. Ma, J. A. Rogers, *Adv. Mater.* **2013**, *25*, 3526.

[7] S.-W. Hwang, G. Park, H. Cheng, J.-K. Song, S.-K. Kang, L. Yin, J.-H. Kim, F. G. Omenetto, Y. Huang, K.-M. Lee, J. A. Rogers, *Adv. Mater.* **2014**, *26*, 1992.

[8] L. Yin, H. Cheng, S. Mao, R. Haasch, Y. Liu, X. Xie, S.-W. Hwang, H. Jain, S.-K. Kang, Y. Su, R. Li, Y. Huang, J. A. Rogers, *Adv. Funct. Mater.* **2014**, *24*, 645.

[9] S.-K. Kang, S.-W. Hwang, H. Cheng, S. Yu, B. H. Kim, J.-H. Kim, Y. Huang, J. A. Rogers, *Adv. Funct. Mater.* **2014**, *24*, 4427.

[10] K. J. Yu, D. Kuzum, S.-W. Hwang, B. H. Kim, H. Juul, N. H. Kim, S. M. Won, K. Chiang, M. Trumpis, A. G. Richardson, H. Cheng, H. Fang, M. Thompson, H. Bink, D. Talos, K. J. Seo, H. N. Lee, S.-K. Kang, J.-H. Kim, J. Y. Lee, Y. Huang, F. E. Jensen, M. A. Dichter, T. H. Lucas, J. Viventi, B. Litt, J. A. Rogers, *Nat. Mater.* **2016**, *15*, 782.

[11] S.-K. Kang, R. K. J. Murphy, S.-W. Hwang, S. M. Lee, D. V. Harburg, N. A. Krueger, J. Shin, P. Gamble, H. Cheng, S. Yu, Z. Liu, J. G. McCall, M. Stephen, H. Ying, J. Kim, G. Park, R. C. Webb, C. H. Lee, S. Chung, D. S. Wie, A. D. Gujar, B. Vemulapalli, A. H. Kim, K.-M. Lee, J. Cheng, Y. Huang, S. H. Lee, P. V. Braun, W. Z. Ray, J. A. Rogers, *Nature* **2016**, *530*, 71.

[12] R. J. Ono, A. L. Z. Lee, Z. X. Voo, S. Venkataraman, B. W. Koh, Y. Y. Yang, J. L. Hedrick, *Biomacromolecules* **2017**, *18*, 2277.

[13] T. Lei, M. Guan, J. Liu, H.-C. Lin, R. Pfattner, L. Shaw, A. F. McGuire, T.-C. Huang, L. Shao, K.-T. Cheng, J. B.-H. Tok, Z. Bao, *Proc. Natl. Acad. Sci. USA* **2017**, *114*, 5107.

[14] M. Maytin, C. A. Henrikson, L. M. Epstein, *Circ.: Arrhythmia Electrophysiol.* **2010**, *3*, 413.

[15] C. M. Boutry, H. Chandrahalim, P. Streit, M. Schinhammer, A. C. Hänzi, C. Hierold, *Philos. Trans. R. Soc., A* **2012**, *370*, 2418.

[16] C. Dagdeviren, S.-W. Hwang, Y. Su, S. Kim, H. Cheng, O. Gur, R. Haney, F. G. Omenetto, Y. Huang, J. A. Rogers, *Small* **2013**, *9*, 3398.

[17] A. Haeberlin, A. Zurbuchen, J. Schaerer, J. Wagner, S. Walpen, C. Huber, H. Haeberlin, J. Fuhrer, R. Vogel, *Europace* **2014**, *16*, 1534.

[18] A. Haeberlin, A. Zurbuchen, S. Walpen, J. Schaerer, T. Niederhauser, C. Huber, H. Tanner, H. Servatius, J. Seiler, H. Haeberlin, J. Fuhrer, R. Vogel, *Heart Rhythm* **2015**, *12*, 1317.

[19] S.-K. Kang, G. Park, K. Kim, S.-W. Hwang, H. Cheng, J. Shin, S. Chung, M. Kim, L. Yin, J. C. Lee, K.-M. Lee, J. A. Rogers, *ACS Appl. Mater. Interfaces* **2015**, *7*, 9297.

[20] J. Yoon, A. J. Baca, S.-I. Park, P. Elvikis, J. B. Geddes, L. Li, R. H. Kim, J. Xiao, S. Wang, T.-H. Kim, M. J. Motala, B. Y. Ahn, E. B. Duoss, J. A. Lewis, R. G. Nuzzo, P. M. Ferreira, Y. Huang, A. Rockett, J. A. Rogers, *Nat. Mater.* **2008**, *7*, 907.

[21] K. Song, J. H. Han, T. Lim, N. Kim, S. Shin, J. Kim, H. Choo, S. Jeong, Y.-C. Kim, Z. L. Wang, J. Lee, *Adv. Healthcare Mater.* **2016**, *5*, 1572.

[22] O. Vetterl, A. Lambertz, A. Dasgupta, F. Finger, B. Rech, O. Kluth, H. Wagner, *Sol. Energy Mater. Sol. Cells* **2001**, *66*, 345.

[23] A. Polman, M. Knight, E. C. Garnett, B. Ehrler, W. C. Sinke, *Science* **2016**, *352*, 307.

[24] K. Yoshikawa, H. Kawasaki, W. Yoshida, T. Irie, K. Konishi, K. Nakano, T. Uto, D. Adachi, M. Kanematsu, H. Uzu, K. Yamamoto, *Nat. Energy* **2017**, *2*, 17032.

[25] L. Yin, A. B. Farimani, K. Min, N. Vishal, J. Lam, Y. K. Lee, N. R. Aluru, J. A. Rogers, *Adv. Mater.* **2015**, *27*, 1857.

[26] S.-W. Hwang, G. Park, C. Edwards, E. A. Corbin, S.-K. Kang, H. Cheng, J.-K. Song, J.-H. Kim, S. Yu, J. Ng, J. E. Lee, J. Kim, C. Yee, B. Bhaduri, Y. Su, F. G. Omennetto, Y. Huang, R. Bashir, L. Goddard, G. Popescu, K.-M. Lee, J. A. Rogers, *ACS Nano* **2014**, *8*, 5843.

[27] P. Gentile, V. Chiono, I. Carmagnola, P. Hatton, *Int. J. Mol. Sci.* **2014**, *15*, 3640.

[28] A. Summerfield, F. Meurens, M. E. Ricklin, *Mol. Immunol.* **2015**, *66*, 14.

[29] K. J. Yu, L. Gao, J. S. Park, Y. R. Lee, C. J. Corcoran, R. G. Nuzzo, D. Chanda, J. A. Rogers, *Adv. Energy Mater.* **2013**, *3*, 1401.

[30] S. Jeong, M. D. McGehee, Y. Cui, *Nat. Commun.* **2013**, *4*, 2950.

[31] C. Trompoukis, O. El Daif, P. Pratim Sharma, H. Sivaramakrishnan Radhakrishnan, M. Debucquoy, V. Depauw, K. Van Nieuwenhuysen, I. Gordon, R. Mertens, J. Poortmans, *Prog. Photovoltaics* **2015**, *23*, 734.

[32] M. A. Karami, D. J. Inman, *Appl. Phys. Lett.* **2012**, *100*, 042901.

[33] C. W. Park, S.-K. Kang, H. L. Hernandez, J. A. Kaitz, D. S. Wie, J. Shin, O. P. Lee, N. R. Sottos, J. S. Moore, J. A. Rogers, S. R. White, *Adv. Mater.* **2015**, *27*, 3783.

[34] B. G. Ribeiro, A. N. Alves, L. A. D. dos Santos, T. M. Cantero, K. P. S. Fernandes, D. d. S. Dias, N. Bernardes, K. De Angelis, R. A. Mesquita-Ferrari, *PLoS One* **2016**, *11*, e0153618.

[35] K. Deisseroth, *Nat. Neurosci.* **2015**, *18*, 1213.

[36] I. S. Aleem, I. Aleem, N. Evaniew, J. W. Busse, M. Yaszemski, A. Agarwal, T. Einhorn, M. Bhandari, *Sci. Rep.* **2016**, *6*, 31724.

1703035 (8 of 8)